NANO LETTERS

Letter

pubs.acs.org/NanoLett

Coherent Coupling of WS_2 Monolayers with Metallic Photonic Nanostructures at Room Temperature

Shaojun Wang,[†] Songlin Li,[†] Thibault Chervy,[†] Atef Shalabney,[†,‡] Stefano Azzini,[†] Emanuele Orgiu,[†] James A. Hutchison,[†] Cyriaque Genet,[†] Paolo Samorì,[†] and Thomas W. Ebbesen*[,†]

[†]University of Strasbourg, CNRS, ISIS & icFRC, Strasbourg 67000, France

[‡]Braude College, Snunit St 51, Karmiel 2161002, Israel

Supporting Information

ABSTRACT: Room temperature strong coupling of WS_2 monolayer exciton transitions to metallic Fabry–Pérot and plasmonic optical cavities is demonstrated. A Rabi splitting of 101 meV is observed for the Fabry–Pérot cavity. The enhanced magnitude and visibility of WS_2 monolayer strong coupling is attributed to the larger absorption coefficient, the narrower line width of the *A* exciton transition, and greater spin–orbit coupling. For WS_2 coupled to plasmonic arrays, the Rabi splitting still reaches 60 meV despite the less favorable coupling conditions, and displays interesting photoluminescence features. The unambiguous signature of WS_2 monolayer strong coupling in easily fabricated metallic resonators at room temperature suggests many possibilities for combining light–matter hybridization with spin and valleytronics.

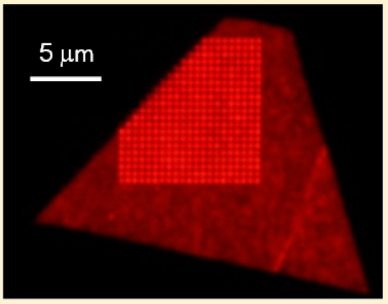

KEYWORDS: *Strong coupling, 2D materials, polaritonics, surface plasmons, WS_2 monolayers*

The strong coupling of light and semiconductor excitons to form exciton–polaritonic states plays a role in many fascinating recent advances, ranging from low-threshold lasing,[1,2] and Bose–Einstein condensation,[3] to enhanced charge transport,[4] workfunction tuning,[5] and phase transition modification.[6] These advances draw on the quasi-bosonic nature of exciton–polaritons and the dispersive and delocalized nature of the hybrid states. The strong coupling limit is reached when coherent energy exchange between the excitonic transition and a resonant optical cavity overcomes other relaxation pathways, the spectral signature of which is the splitting of the absorption band corresponding to the two polaritonic states.[7−9] The splitting of these states at resonance, i.e., the Rabi splitting, $\hbar\Omega_R$, measures the coupling strength and depends on the scalar product of the electric field per photon $\boldsymbol{E}$ in the cavity and the exciton transition dipole moment $\boldsymbol{d}$.

The choice of appropriate optical cavity and semiconductor transition always involves a compromise between maximizing the $\boldsymbol{E}\cdot\boldsymbol{d}$ product while minimizing losses. On the photonic side, this typically lies in the choice of either distributed Bragg reflectors (DBRs) with high Q factors but diffuse mode volumes, or metallic resonators that concentrate the optical field in subwavelength volumes but suffer absorption losses. On the excitonic side, one ideally seeks a highly allowed (direct band gap) dipolar transition in the visible/near-IR spectral region forming a tightly bound energy exciton for room temperature stability, with minimal nonradiative relaxation pathways and inhomogeneous broadening. Monolayer transition metal dichalcogenides (TMDs) exhibit excitonic transitions that satisfy all these criteria.

During the past five years, it has been demonstrated that group VI TMDs with structure MX_2 (where M is Mo or W and X is S or Se) display a transition from indirect to direct band gap semiconductors when passing from multilayers to a monolayer.[10−12] The resulting strongly allowed excitonic resonances dominate the visible and near-IR absorption spectra of these systems, having exceptionally large binding energies (>0.3 eV) due to the reduced dielectric screening.[13−15] The absorption coefficients in 2D TMDs monolayers can reach up to 1.0×10^6 cm^{-1}, much higher than those of typical colloidal CdSe quantum dots (0.2×10^5 cm^{-1}),[16] and comparable to very high density layers of organic dye aggregates (e.g., cyanine J-aggregates, 0.5×10^6 cm^{-1}).[17] Figure 1a shows a top view of the WS_2 monolayer. The direct band gap transition in the monolayer case occurs at the energy-degenerate K (K′) points at the edges of the 2D hexagonal Brillouin zone.[18−21] Monolayer TMDs exhibit emission yields approaching unity in the absence of surface trap states,[22] which is important for lasing[23] and other optoelectronic applications.[24−26]

Recently the first reports of strong light–matter coupling with monolayer TMDs appeared in literature, all involving MoX_2 monolayers. Menon and co-workers[27] and Tartakovskii and co-workers[28] incorporated MoS_2 and $MoSe_2$, respectively, into DBR cavities, while Agarwal and co-workers[29] recently studied the coupling of MoS_2 to both local and surface lattice modes of metal nanoparticle arrays. These studies show the real potential of MoX_2 TMDs for strong coupling, but the observed

Received: April 9, 2016
Revised: May 24, 2016
Published: June 6, 2016

ACS Publications © 2016 American Chemical Society

DOI: 10.1021/acs.nanolett.6b01475
Nano Lett. 2016, 16, 4368−4374

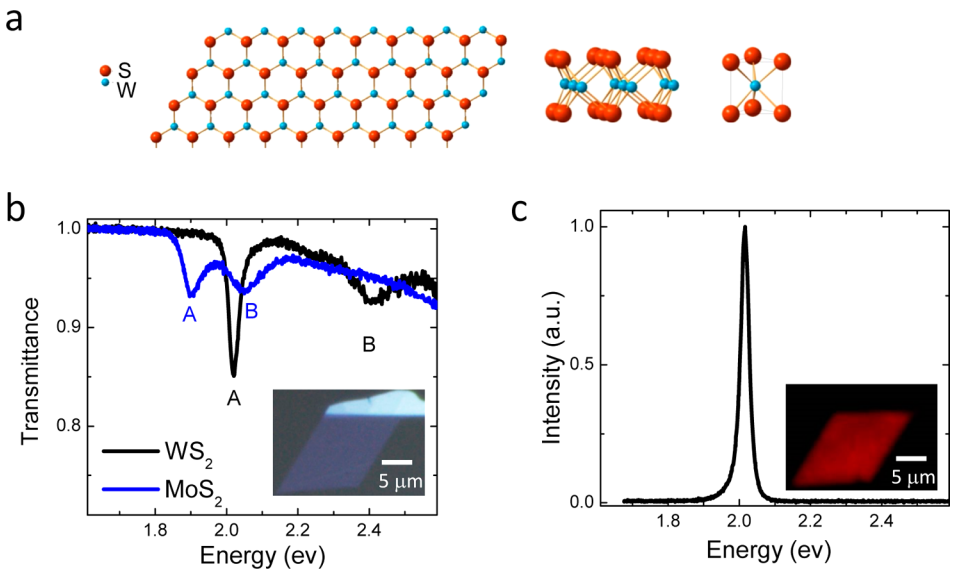

Figure 1. (a) Structure of a WS_2 monolayer showing, from left to right, out-of-plane view, in-plane view, and the unit cell. (b) Transmittance of monolayers of WS_2 (black solid curve) and MoS_2 (blue solid curve) on quartz; the inset shows an optical micrograph of the WS_2 flake in which the blue region is a monolayer and the bright region is a multilayer. (c) Emission spectrum taken from the monolayer region of WS_2 under continuous wave (cw) 532 nm (2.330 eV) excitation. The inset displays the fluorescence image of the WS_2 flake in which bright emission is observed only from the monolayer region under cw 470 ± 10 nm (2.64 ± 0.06 eV) excitation.

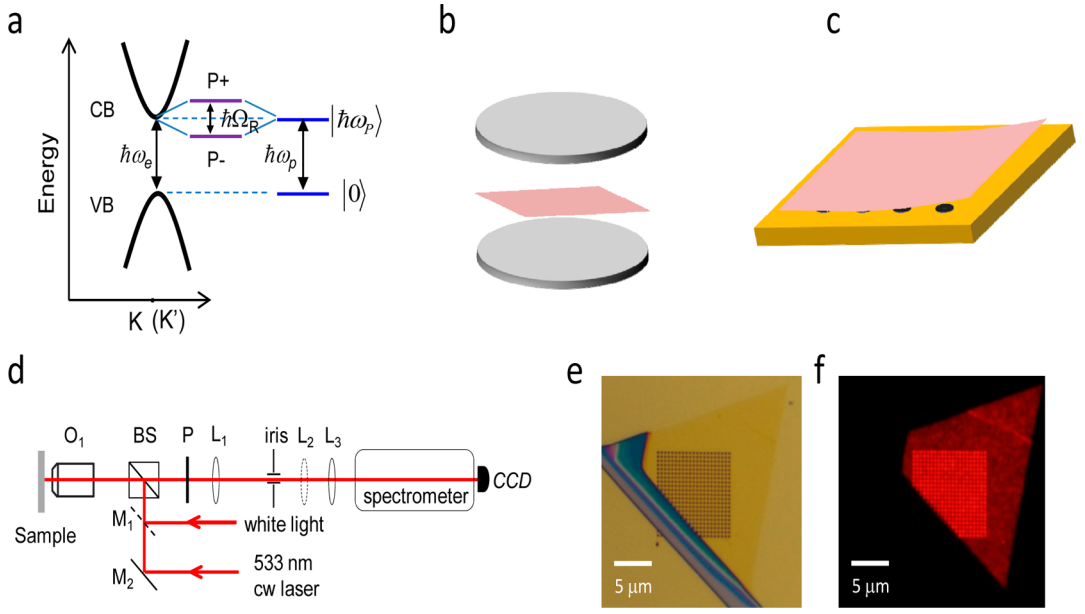

Figure 2. (a) Energy diagram of the strong coupling of the direct band gap transition $\hbar\omega_e$ between the valence band (VB) and conductive band (CB) of monolayer WS_2 to the first optical mode $\hbar\omega_p$ of a cavity. The coherent coupling forms two polaritonic states P+ and P− separated by the Rabi energy $\hbar\Omega_R$. (b) Schematic of the Ag Fabry−Perot (FP) cavity with WS_2 monolayer placed at the center (the optical field maximum). (c) Schematic of the plasmonic hole array with WS_2 monolayer physisorbed on top. Five nanometers of PMMA separates the monolayer from the metal surface. (d) Schematic of the optical setup for angle resolved spectroscopy. White light source or cw 533 nm laser beam is selected by the flipped mirror M_1 to pass through a beam splitter (BS) and a 40× objective lens (O_1, N.A. = 0.6). The reflected beam or PL from the sample, collected by the same O_1, passes through a polarization analyzer (P), tube lens (L_1), spatial filtering iris, imaging lens (formed by L_2 and L_3), Fourier lens (L_3), and spectrometer coupled CCD. (e) Optical micrograph of a WS_2 monolayer physisorbed on the plasmonic hole array; the monolayer region is delineated by the red PL image of the same WS_2 monolayer in (f).

Rabi splittings were limited by the absorption features of the materials with a maximum reported splitting of 86 meV at room temperature.[29] Furthermore, in MoX_2 monolayers, spin−orbit coupling (SOC) induces the splitting of the excitonic transition by ca. 150 meV such that both the so-called *A* and *B* exciton transitions (see Figure 1b) can simultaneously interact with cavity modes complicating the studies of such systems.[29] The WS_2 monolayer has the advantage that it presents a much sharper isolated absorption band as can be seen in Figure 1b. In addition it displays an intense photoluminescence (PL) peak at 2.016 eV (Figure 1c). Hence WS_2 constitutes a natural choice for light−matter strong coupling.

In this letter we demonstrate that, by coupling WS_2 monolayers to metallic resonators, the magnitude and visibility

DOI: 10.1021/acs.nanolett.6b01475
Nano Lett. 2016, 16, 4368−4374

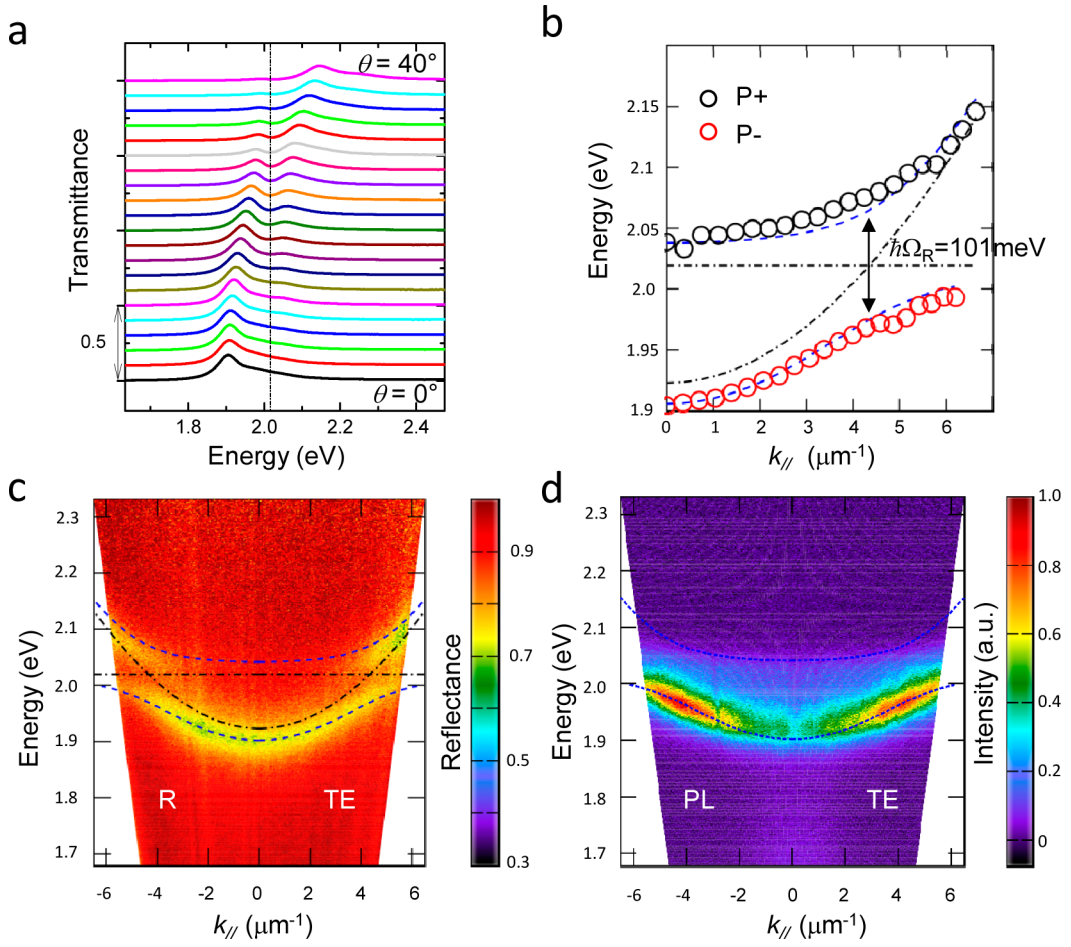

Figure 3. (a) Transmission spectra as a function of probe angle (θ from 0° to 40°) for a FP cavity with the monolayer WS_2. (b) Peak transmission energies as a function of in-plane angular momentum for the same FP cavity. Black and red circles correspond, respectively, to the measured positions of the P+ and P− extracted from the data displayed in a. Black horizontal dot-dashed line and curves show, respectively, the dispersion of the A exciton transition energy and empty cavity mode. The P+ and P− band are fitted by blue dashed curves using coupled oscillator model (see Methods). (c) Energy/in-plane momentum dispersion for the same FP cavity taken in TE reflection mode. (d) Dispersion of the photoluminescence from the same FP cavity under cw 532 nm excitation. The energies of P+ and P− bands are indicated, taken from c.

of light−monolayer TMD strong coupling at room temperature are enhanced with a Rabi splitting of 101 meV in Fabry−Pérot (FP) cavities and 60 meV on plasmonic arrays. The energy−momentum dispersion properties of the monolayer WS_2 exciton−polaritons are explored by transmission, reflection, and photoluminescence (PL) spectroscopy. In particular Rabi splittings in TE and TM dispersion curves give rise to unusual PL behavior. The results are discussed in terms of the potential of coherent light−matter interactions using WS_2 monolayers.

To ensure high quality samples and to avoid environmental contamination, the TMD monolayers were exfoliated from bulk single crystals and then dry-transferred onto substrates as described in the Methods section. The *A* exciton of monolayer WS_2 absorbs 14% of normally incident unpolarized light, ca. 2.5 times more than a monolayer MoS_2 (calculated from imaginary refractive index in SI, Figure S2). The stronger SOC-induced splitting of the *A* and *B* bands in WS_2 (ca. 389 meV) is also clear, as is the narrower line width of the *A* exciton (28 meV) compared to that of monolayer MoS_2 (45 meV, see SI, Tables S1 and S2). The WS_2 monolayer emission quantum yield, in the absence of special surface treatment methods,[22] was estimated to be 6% by others.[31] The exciton emission (2.016 eV) has a line width of 26 meV, displaying a tiny Stokes shift (~4 meV) from the *A* exciton absorption. All emission studies herein were conducted at the minimum pump intensity possible (less than 1.0 $\mu W/\mu m^2$) such that many-body interactions were avoided.[31,32]

Figure 2a illustrates the generic coupling of a 2D material to resonant optical mode leading to the formation of the polaritonic states P+ and P− separated by the Rabi splitting. $\hbar\Omega_R$ remains finite even in absence of real photons due to interaction with the zero-point energy fluctuations (vacuum field) of the confined electromagnetic field. In this study WS_2 monolayers were coupled to two types of metallic resonators: FP cavities and periodic plasmonic structures. First, we fabricated FP cavities with mirrors of 50 nm of Ag and the WS_2 monolayer was positioned at the field maximum[17] at the center of the cavity with ±5 nm accuracy using LiF spacer layers (see schematic, Figure 2b). The cavity thickness was adjusted such that its fundamental mode was tuned to the *A* exciton energy ensuring the smallest mode volume.[17]

Second, a WS_2 monolayer was transferred onto hole arrays milled by focused ion beam in a Au film (see schematic in Figure 2c). A 5 nm PMMA film was spin coated onto the array first to avoid emission quenching,[33] or hot electron transfer between Au and the semiconductor;[34,35] nevertheless, the monolayer is still positioned near the plasmonic field maximum at the interface. The surface plasmon (SP) resonance was tuned

DOI: 10.1021/acs.nanolett.6b01475
Nano Lett. 2016, 16, 4368−4374

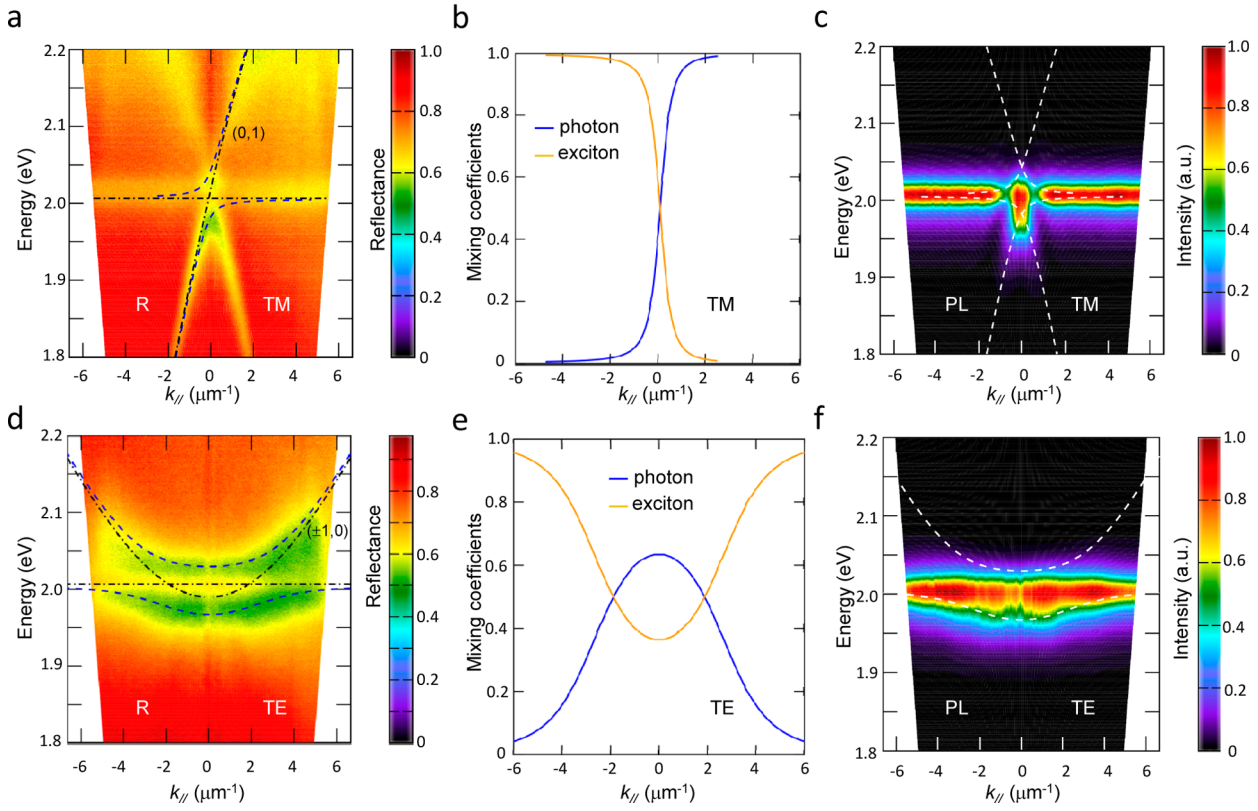

Figure 4. (a,d) Energy/in-plane momentum dispersion for the plasmonic hole array with WS_2 monolayer taken in TM and TE reflection mode, respectively. Black horizontal dot-dashed line and curves show, respectively, the dispersion of the A exciton transition energy and empty SP (0, ±1)/(±1, 0) mode. The P+ and P− band are fitted by blue dashed curves using coupled oscillator model (see Methods). For clarity, (a) only shows the results for the (0, 1) branch. (b,e) The mixing coefficients of P− band shown in a and d. Blue and yellow curves represent the photon and exciton content of the P− band, respectively. (c,f) Dispersion of the photoluminescence from the same plasmonic hole array. The energies of P+ and P− bands are indicated, taken from a and d.

to the A exciton energy by adjusting the array period[36] (e.g., a period of 530 nm gives a surface plasmon resonance near 2.010 eV when a monolayer flake is on top). An optical micrograph and PL image clearly show the position of the WS_2 monolayer on top of a hole array (Figure 2e,f). The emission is enhanced ~2.5-fold above the holes possibly due to two factors: first, the plasmonic field has a maximum above the holes, enhancing the photonic mode density at this point, thereby increasing the excitonic radiative rate,[33] and second, the increased dielectric screening where the monolayer is suspended over the hole rather than in van der Waals contact with the substrate could enhance the emission.[10]

Angle-resolved transmission spectra of the FP cavity with WS_2 monolayer are shown in Figure 3a for TE polarization. The progressive dispersion of the cavity mode through the energy of the *A* exciton is accompanied by a clear anticrossing, which is mapped out in terms of spectral maxima in Figure 3b. After fitting the energy of the two peaks as a function of in-plane momentum $k_{||}$ using the coupled oscillator model (described in the Methods), it is evident that the original exciton transition energy (black horizontal dot-dashed line in Figure 3b) and the cavity mode (black parabolic dot-dashed curve) split into two new bands, P+ and P− (blue dashed curves). Both the experimental data and the fitted curves unambiguously demonstrate an anticrossing effect, resulting from the coupling between the fundamental cavity mode and the *A* exciton transition. From the fitting a Rabi splitting of 101 meV is extracted. This splitting is greater than the line width of the FP cavity mode (~80 meV, SI Figure S4a) and the exciton line width (28 meV) putting the interaction firmly in the strong coupling regime. The relative photonic and excitonic content of the polariton states can be calculated in terms of mixing coefficients, given in SI, Figure S5, as a function of the in-plane momentum $k_{||}$. The results show that the polaritonic states are 1:1 hybrids of the *A* exciton and the cavity at $|k_{||}| = 4.35\ \mu m^{-1}$. The dispersion of the sample also was measured in Fourier space by microscope reflectometry (schematized in Figure 2d), and the results are shown in Figure 3c. The Rabi splitting, again extracted from a coupled oscillator model, was 90 meV, a little smaller than that observed in transmission measurements, as expected.[37] The Fourier image of the photoluminescence from the same cavity is shown in Figure 3d. The emission from the lower branch polariton clearly dominates, but emission is also observed at the uncoupled exciton energy (Stokes shift 4 meV), while upper branch polariton emission is not detected. Notice that the P− emission is centered at $k_{||}$ values where the bare optical mode is iso-energetic with the *A* exciton.

The dispersion curves of the plasmonic hole array with a monolayer WS_2 in both TM and TE modes are shown in Figure 4, while the bare plasmonic hole array dispersion are reported in SI, Figure S4b. Under TM polarization, the anticrossing between the (0, ±1) SP modes (black dot-dashed curves in Figure 4a) and the *A* exciton (horizontal black dot-dashed line in Figure 4a) is again clear, giving a Rabi splitting of 60 meV. This value is smaller than the one observed for the FP cavity but still easily observable given the width of the SP

DOI: 10.1021/acs.nanolett.6b01475
Nano Lett. 2016, 16, 4368−4374

resonance at 2.010 eV (36 meV). This reduction of Rabi splitting in going from FP cavities to plasmonic hole arrays is much greater than that observed in previous studies with disordered molecular layers.[37] Indeed, the exciton transition dipole is oriented in-plane in TMD monolayers, thus perfectly aligned with the field polarization of the FP cavity (Figure 2b), whereas for the plasmonic arrays the field is elliptically polarized at the interface, reducing the scalar product of $\boldsymbol{E}$ and $\boldsymbol{d}$.

The mixing coefficients for the strong coupling of the (0, −1) TM mode and the exciton in Figure 4b shows that the interaction between them is limited to an in-plane momentum range of −1 to 1 μm^{-1} due to the strongly dispersive behavior of the TM mode. This has consequence for the emission as can be seen in Figure 4c. At the anticrossing, the emission is mainly a mixture of the bare and coupled WS_2 (see the solid blue curve in SI, Figure S6a). A weak shoulder can be observed at the position of higher branch polariton compared the emission of uncoupled exciton.

In the TE case, an anticrossing with a Rabi splitting of 60 meV is also observed for the interaction of the (±1, 0) SP mode with the WS_2 monolayer (Figure 4d) even though the quality factor of the bare TE SP mode is a bit lower ($Q \approx 20$ at 2.010 eV). The dispersion of the TE mode has a parabolic shape as shown in Figure 4d (dot-dashed curves). The slower dispersion of this mode results in a larger range of interacting in-plane momenta, from −5 to 5 μm^{-1}. In the range −2 to 2 μm^{-1}, the measured P+ and P− bands are fitted well by the coupled oscillator model. However, beyond this range P+ bends downward due to interactions with the higher (1, 1) SP modes, which are not included in the model. The dispersion of P− emission (Figure 4f) also matches well with the predictions of the coupled oscillator model. At the resonant condition, $k_{\|} = \pm 1.89\ \mu m^{-1}$, the PL spectrum in SI, Figure S6b, is dominated by the uncoupled exciton, with weak emission from P+ and P−.

The hint of emission from the upper polariton branch observed here for the plasmonic array (TM polarization) recalls the observation of emission from the upper branch in DBR cavities with MoX_2 monolayer.[27,28] Tartakovskii and co-workers[28] point out that the ratio of the Rabi splitting to the exciton binding energy is unusually small in these systems, 0.04 in their case compared to a ratio >0.2 in all other strongly coupled systems ever studied. Therefore, the electron−hole continuum lies far from the polariton resonances and does not efficiently dephase them. Taking literature estimates for the exciton binding energy in WS_2 (0.3−0.7 eV),[13−15] the same ratio observed here takes values in between 0.15 and 0.37 for the FP cavity and 0.09−0.22 for the plasmonic array. The unusual gaps in the PL under TM polarization near $k_{\|} = 0$ most likely originate from the competition between the different modes of density in TM and TE that coexist at this momentum. Another interesting difference between the TM and TE dispersion curves lies in the curvature of the P− branch, which concave in the case of TE, while sharply convex for TM. This should have dramatic effects on the polariton dynamics in such systems. For instance, BEC can only be achieved in the TE case as it requires a stable minimum to accumulate population. Future studies of ultrafast dynamics of these systems will provide more insight into such issues.

In summary we have shown that by incorporating WS_2 monolayers into metallic optical nanocavities, clear signatures of strong coupling are observed in transmission, reflection, and emission at room temperature. While metallic FP cavities give larger Rabi splittings for this material, plasmonic cavities (either local SPs on nanoparticles[38] or diffractive modes on arrays[39]) are open and thus easily integrated into optoelectronic devices and also accessible for chemical applications. Recent work has demonstrated that a chemical reaction rate can be controlled by excitonic light−matter strong coupling.[40] It has been suggested that such effects can be extended to coupling vibrational modes of specific bonds.[41] Our findings are therefore also particularly relevant given that WS_2 and other TMDs are widely exploited materials for applications in catalysis. Finally, the results here suggest that the combination of the already rich spin and valley physics of monolayer TMDs with polariton physics at room temperature should open exciting possibilities in fundamental physics.

Methods. *Sample Fabrication.* Atomically thin MoS_2 and WS_2 films were fabricated by an improved mechanical exfoliation method[42] from a synthetic single crystal (hq graphene, The Netherlands), and the monolayer samples were identified by optical contrast, absorption, and PL spectroscopy. The monolayer WS_2 flakes were first deposited on a flexible PDMS slab before being transferred onto the substrates (such as quartz, cavity).[6] Beginning with FP metallic cavities, a 50 nm thick silver film was evaporated on a glass substrate, upon which was evaporated an 86 nm-thick LiF film. Subsequently, the monolayer WS_2 flake was transferred onto this half metallic FP cavity substrate. Ninety nanometer-thick LiF and 50 nm-thick Ag film were subsequently evaporated onto the flake surface to form a medium quality (Q factor ∼30 at 614 nm) FP cavity. For plasmonic samples, subwavelength hole arrays were milled by focused ion beam (FIB) in sputtered gold films of 260 nm thickness on a glass substrate covered by a 5 nm thick chromium adhesion layer. The hole diameter and the period of the hole array were 120 and 530 nm, respectively (shown in the SEM image of Figure S1). To avoid short-range interactions between the flake and gold, a 5 nm thick of PMMA film was deposited onto the hole array. Finally, the monolayer flake on a PDMS slab was transferred onto the hole array under microscope.

Optical Measurements. The transmission spectra of the monolayer flakes on quartz substrate and FP cavity samples were measured using an optical microscope. The samples were aligned along the optical axis of the microscope and illuminated with quasi-collimated white light. The light transmitted by the samples was then collected using a microscope objective lens (20× magnification, N.A. = 0.45) and imaged by a spectrometer (Acton SpectraPro 300i) and silicon charge-couple-device (CCD) (Princeton Instrument VersArray 1300B). The angular dispersion of FP cavity samples was characterized with the transmission goniometric method by rotating the samples from the normal incidence condition to 40° by every 2°. Meanwhile, the reflection and PL spectra of all the samples were measured using a microscope reflectometry setup equipped with an optical Fourier analysis lens (L_3 shown in Figure 2d). In this setup, the samples were excited by white light or 533 nm laser beam. A 40× objective (N.A. = 0.60) collected the emission or transmission, directing it to an iris at the focus point of the tube lens (L_1). The iris acts as a spatial filter selecting a $\sim 5 \times 5\ \mu m^2$ area of the sample plane. The angular distribution of the reflection or emission from the sample was analyzed in the Fourier plane of L_3. A white light beam and lens L_2 in the optical path were used as a microscope to locate samples in real space. A linear polarizer was placed in front of L_1 to select either TE or TM mode of the cavity samples.

DOI: 10.1021/acs.nanolett.6b01475
Nano Lett. 2016, 16, 4368−4374

Dispersion of 2D Material Calculated by Multi-Lorentzian Model. The optical properties of WS_2 monolayer was analyzed using a multi-Lorentzian model in order to simulate WS_2−cavity interactions using transfer matrices, as described below and in the SI for the details. The findings were systematically compared to the MoS_2 system. The refractive index of WS_2 extracted from transmission measurements are included in the SI, Figure S2, together with fitted functions from which oscillator strengths and line widths were extracted (SI, Tables S1 and S2). Our estimated dielectric functions are in good qualitative agreement with the literature.[30] The WS_2−cavity results (displayed in Figure S3) reveal a Rabi splitting being ∼1.5- fold that of MoS_2, a value comparable to the ratio of their transition dipole moments.

The dispersion of the WS_2 and MoS_2 monolayers was retrieved from the transmission measurements using a multi-Lorentzian model.[30,41] The absorption bands were represented by multiple resonances as $\varepsilon(E) = \varepsilon_B + \sum_{j=1}^{N} \frac{f_j}{E_{0j}^2 - E^2 - iE\cdot\Gamma_j}$, E being the photon energy in eV, whereas ε_B, f_j, E_{0j}, and Γ_j are, respectively, the background dielectric contribution, oscillator strength, resonance energy, and the phenomenological damping constant of absorption band j. The absorption intensity of the band is determined by both f_j and Γ_j, whereas the line width is solely governed by Γ_j. In the fit procedure, all these parameters together were varied to obtain the best fit with the experimental measurements. The thicknesses of the WS_2 and MoS_2 monolayers were considered as 0.618 and 0.646 nm, respectively.[30] Since monolayer structures are considered, ε_B can be reasonably assumed as unity ($\varepsilon_B = 1$). To account for the substrate refractive index, the reflectivity and transmittance of the single interface was calculated from the measured transmission of the bare quartz substrate. The dispersion parameters of monolayer WS_2 and MoS_2 are given in the Tables S1 and S2 of SI, respectively.

Dispersion Curves Fitted by the Coupled Oscillator Models. The polariton dispersion extracted from the transmittance maxima or the reflectivity minima are fitted by a coupled oscillator model:[8] $\begin{bmatrix} E_{ph}(k_\parallel) & V \\ V & E_{ex} \end{bmatrix} \begin{pmatrix} \alpha \\ \beta \end{pmatrix} = E_{pol}(k_\parallel) \begin{pmatrix} \alpha \\ \beta \end{pmatrix}$, where $E_{ph}(k_\parallel)$ is the energy of empty photonic mode, $V = \hbar\Omega_R/2$ the interaction potential between photonic mode and exciton with energy E_{ex}, and $E_{pol}(k_\parallel)$ the momentum dependent hybrid eigenvalues of P+ and P− branches. The mixing coefficients $|\alpha|^2$ and $|\beta|^2$ describe the relative photonic and excitonic content of the polaritonic states, and α,β are known as the Hopfield coefficients. For the plasmonic hole array, the dispersion of SP modes are defined by the momentum matching condition as

$$|\vec{k}_{spp}| = \left| \vec{i}\left(m\frac{2\pi}{P}\right) + \vec{j}\left(n\frac{2\pi}{P} + k_\parallel\right) \right| \quad (1)$$

where $\vec{i}$, $\vec{j}$ are unit vectors along horizontal and vertical directions, respectively, $k_\parallel$ is the in-plane momentum component of the incident light, P is the lattice period, and m and n are integers. The scattering orders of SP modes are denoted by (m, n). From eq 1, the dispersion of degenerated TE $(\pm1, 0)$ mode can be written as

$$\omega = \frac{c}{n_{sp}}\sqrt{k_\parallel^{\,2} + \left(\frac{2\pi}{P}\right)^2} \quad (2)$$

where ω is the light frequency, c the propagation speed of the light in the vacuum, and n_{sp} the effective index of SP modes ($n_{sp} = \sqrt{\frac{\varepsilon_m\varepsilon_d}{\varepsilon_m + \varepsilon_d}}$, ε_m and ε_d are the permittivities of Au film and air). When $-\frac{2\pi}{P} \le k_\parallel \le \frac{2\pi}{P}$, the dispersion of TM (0, 1) and (0, −1) mode are, respectively, described as

$$\omega = \frac{c}{n_{sp}}\left(k_\parallel + \frac{2\pi}{P}\right) \quad (3)$$

$$\omega = -\frac{c}{n_{sp}}\left(k_\parallel - \frac{2\pi}{P}\right) \quad (4)$$

■ ASSOCIATED CONTENT

Supporting Information

The Supporting Information is available free of charge on the ACS Publications website at DOI: 10.1021/acs.nanolett.6b01475.

Scanning electron microscope (SEM) image of the hole array sample, refractive index and dispersion parameters of monolayer of 2D materials, bare optical modes, comparison of transmission and reflection of coupled FP cavities simulated by transfer matrix method, mixing coefficients of strongly coupled monolayer WS_2 with the TE mode of FP cavity, and PL spectra of strong coupled monolayer WS_2 with TM/TE mode of hole array (PDF)

■ AUTHOR INFORMATION

Corresponding Author

*E-mail: ebbesen@unistra.fr.

Author Contributions

S.W., S.L., and T.C. authors contributed equally to this work.

Notes

The authors declare no competing financial interest.

■ ACKNOWLEDGMENTS

This work was supported by the European Commission through the Graphene Flagship (GA-604391) and the FET project UPGRADE (grant no. 309056), the ANR Equipex Union (ANR-10-EQPX-52-01), the Labex NIE projects (ANR-11-LABX-0058 NIE), and CSC (ANR-10-LABX-0026 CSC) within the Investissement d'Avenir program ANR-10-IDEX-0002-02, the International Center for Frontier Research in Chemistry (icFRC).

■ REFERENCES

(1) Deng, H.; Weihs, G.; Snoke, D.; Bloch, J.; Yamamoto, Y. *Proc. Natl. Acad. Sci. U. S. A.* **2003**, *100* (26), 15318−15323.

(2) Kena-Cohen, S.; Forrest, S. R. *Nat. Photonics* **2010**, *4* (6), 371−375.

(3) Kasprzak, J.; Richard, M.; Kundermann, S.; Baas, A.; Jeambrun, P.; Keeling, J. M. J.; Marchetti, F. M.; Szymanska, M. H.; Andre, R.; Staehli, J. L.; Savona, V.; Littlewood, P. B.; Deveaud, B.; Dang, L. S. *Nature* **2006**, *443* (7110), 409−414.

(4) Orgiu, E.; George, J.; Hutchison, J. A.; Devaux, E.; Dayen, J. F.; Doudin, B.; Stellacci, F.; Genet, C.; Schachenmayer, J.; Genes, C.; Pupillo, G.; Samori, P.; Ebbesen, T. W. *Nat. Mater.* **2015**, *14*, 1123−1129.

(5) Hutchison, J. A.; Liscio, A.; Schwartz, T.; Canaguier-Durand, A.; Genet, C.; Palermo, V.; Samori, P.; Ebbesen, T. W. *Adv. Mater.* **2013**, *25* (17), 2481−2485.

DOI: 10.1021/acs.nanolett.6b01475
Nano Lett. 2016, 16, 4368−4374

(6) Wang, S.; Mika, A.; Hutchison, J. A.; Genet, C.; Jouaiti, A.; Hosseini, M. W.; Ebbesen, T. W. *Nanoscale* **2014**, *6* (13), 7243−7248.
(7) Haroche, S.; Kleppner, D. *Phys. Today* **1989**, *42* (1), 24−30.
(8) Raimond, J.-M.; Haroche, S. *Exploring the Quantum*; Oxford University Press: Oxford, 2006.
(9) Torma, P.; Barnes, W. L. *Rep. Prog. Phys.* **2015**, *78* (1), 013901.
(10) Mak, K. F.; Lee, C.; Hone, J.; Shan, J.; Heinz, T. F. *Phys. Rev. Lett.* **2010**, *105* (13), 136805.
(11) Splendiani, A.; Sun, L.; Zhang, Y. B.; Li, T. S.; Kim, J.; Chim, C. Y.; Galli, G.; Wang, F. *Nano Lett.* **2010**, *10* (4), 1271−1275.
(12) Ramakrishna Matte, H. S. S.; Gomathi, A.; Manna, A. K.; Late, D. J.; Datta, R.; Pati, S. K.; Rao, C. N. R. *Angew. Chem., Int. Ed.* **2010**, *49* (24), 4059−4062.
(13) Chernikov, A.; Berkelbach, T. C.; Hill, H. M.; Rigosi, A.; Li, Y.; Aslan, O. B.; Reichman, D. R.; Hybertsen, M. S.; Heinz, T. F. *Phys. Rev. Lett.* **2014**, *113* (7), 076802.
(14) Liu, H.-L.; Shen, C.-C.; Su, S.-H.; Hsu, C.-L.; Li, M.-Y.; Li, L.-J. *Appl. Phys. Lett.* **2014**, *105* (20), 201905.
(15) Zhu, B.; Chen, X.; Cui, X. *Sci. Rep.* **2015**, *5*, 9218.
(16) Gomez, D. E.; Vernon, K. C.; Mulvaney, P.; Davis, T. J. *Nano Lett.* **2010**, *10*, 274−278.
(17) Wang, S.; Chervy, T.; George, J.; Hutchison, J. A.; Genet, C.; Ebbesen, T. W. *J. Phys. Chem. Lett.* **2014**, *5* (8), 1433−1439.
(18) Cao, T.; Wang, G.; Han, W. P.; Ye, H. Q.; Zhu, C. R.; Shi, J. R.; Niu, Q.; Tan, P. H.; Wang, E.; Liu, B. L.; Feng, J. *Nat. Commun.* **2012**, *3*, 887.
(19) Xu, X. D.; Yao, W.; Xiao, D.; Heinz, T. F. *Nat. Phys.* **2014**, *10* (5), 343−350.
(20) Rivera, P.; Seyler, K. L.; Yu, H. Y.; Schaibley, J. R.; Yan, J. Q.; Mandrus, D. G.; Yao, W.; Xu, X. D. *Science* **2016**, *351* (6274), 688−691.
(21) Xiao, D.; Liu, G.-B.; Feng, W.; Xu, X.; Yao, W. *Phys. Rev. Lett.* **2012**, *108* (19), 196802.
(22) Amani, M.; Lien, D. H.; Kiriya, D.; Xiao, J.; Azcatl, A.; Noh, J.; Madhvapathy, S. R.; Addou, R.; Santosh, K. C.; Dubey, M.; Cho, K.; Wallace, R. M.; Lee, S. C.; He, J. H.; Ager, J. W.; Zhang, X.; Yablonovitch, E.; Javey, A. *Science* **2015**, *350* (6264), 1065−1068.
(23) Ye, Y.; Wong, Z. J.; Lu, X. F.; Ni, X. J.; Zhu, H. Y.; Chen, X. H.; Wang, Y.; Zhang, X. *Nat. Photonics* **2015**, *9*, 733−737.
(24) Ross, J. S.; Klement, P.; Jones, A. M.; Ghimire, N. J.; Yan, J. Q.; Mandrus, D. G.; Taniguchi, T.; Watanabe, K.; Kitamura, K.; Yao, W.; Cobden, D. H.; Xu, X. D. *Nat. Nanotechnol.* **2014**, *9* (4), 268−272.
(25) Li, Y.; Rao, Y.; Mak, K. F.; You, Y.; Wang, S.; Dean, C. R.; Heinz, T. F. *Nano Lett.* **2013**, *13* (7), 3329−3333.
(26) Sie, E. J.; McIver, J. W.; Lee, Y.-H.; Fu, L.; Kong, J.; Gedik, N. *Nat. Mater.* **2014**, *14* (3), 290−294.
(27) Liu, X.; Galfsky, T.; Sun, Z.; Xia, F.; Lin, E.-c.; Lee, Y.-H.; Kéna-Cohen, S.; Menon, V. M. *Nat. Photonics* **2014**, *9* (1), 30−34.
(28) Dufferwiel, S.; Schwarz, S.; Withers, F.; Trichet, A. A. P.; Li, F.; Sich, M.; Del Pozo-Zamudio, O.; Clark, C.; Nalitov, A.; Solnyshkov, D. D.; Malpuech, G.; Novoselov, K. S.; Smith, J. M.; Skolnick, M. S.; Krizhanovskii, D. N.; Tartakovskii, A. I. *Nat. Commun.* **2015**, *6*, 8579.
(29) Liu, W.; Lee, B.; Naylor, C. H.; Ee, H.-S.; Park, J.; Johnson, A. T. C.; Agarwal, R. *Nano Lett.* **2016**, *16* (2), 1262−1269.
(30) Li, Y. L.; Chernikov, A.; Zhang, X.; Rigosi, A.; Hill, H. M.; van der Zande, A. M.; Chenet, D. A.; Shih, E. M.; Hone, J.; Heinz, T. F. *Phys. Rev. B: Condens. Matter Mater. Phys.* **2014**, *90* (20), 205422.
(31) Yuan, L.; Huang, L. B. *Nanoscale* **2015**, *7* (16), 7402−7408.
(32) Kim, M. S.; Yun, S. J.; Lee, Y.; Seo, C.; Han, G. H.; Kim, K. K.; Lee, Y. H.; Kim, J. *ACS Nano* **2016**, *10* (2), 2399−2405.
(33) Barnes, W. *J. Mod. Opt.* **1998**, *45* (4), 661−699.
(34) Brongersma, M. L.; Halas, N. J.; Nordlander, P. *Nat. Nanotechnol.* **2015**, *10* (1), 25−34.
(35) Li, Z.; Xiao, Y.; Gong, Y.; Wang, Z.; Kang, Y.; Zu, S.; Ajayan, P. M.; Nordlander, P.; Fang, Z. *ACS Nano* **2015**, *9* (10), 10158−10164.
(36) Genet, C.; Ebbesen, T. W. *Nature* **2007**, *445* (7123), 39−46.
(37) Schwartz, T.; Hutchison, J. A.; Genet, C.; Ebbesen, T. W. *Phys. Rev. Lett.* **2011**, *106* (19), 196405.
(38) Zengin, G.; Wersäll, M.; Nilsson, S.; Antosiewicz, T. J.; Käll, M.; Shegai, T. *Phys. Rev. Lett.* **2015**, *114* (15), 157401.
(39) Rodriguez, S. R. K.; Feist, J.; Verschuuren, M. A.; Garcia Vidal, F. J.; Gomez Rivas, J. G. *Phys. Rev. Lett.* **2013**, *111* (16), 166802.
(40) Hutchison, J. A.; Schwartz, T.; Genet, C.; Devaux, E.; Ebbesen, T. W. *Angew. Chem., Int. Ed.* **2012**, *51* (7), 1592−1596.
(41) Shalabney, A.; George, J.; Hutchison, J.; Pupillo, G.; Genet, C.; Ebbesen, T. W. *Nat. Commun.* **2015**, *6*, 5981.
(42) Li, S.-L.; Komatsu, K.; Nakaharai, S.; Lin, Y.-F.; Yamamoto, M.; Duan, X.; Tsukagoshi, K. *ACS Nano* **2014**, *8* (12), 12836−12842.

DOI: 10.1021/acs.nanolett.6b01475
Nano Lett. 2016, 16, 4368−4374